This is a preprint, the final version is subject to change, of the American Mineralogist (MSA)
Cite as Authors (Year) Title. American Mineralogist, in press.
(DOI will not work until issue is live.) DOI: http://dx.doi.org/10.2138/am-2015-5062

Cation order-disorder in Fe-bearing pyrope and grossular garnets: An ^{27}Al and ^{29}Si MAS NMR and ^{57}Fe Mössbauer spectroscopy study

REVISION 1

Aaron C. Palke[1,*,#], Jonathan F. Stebbins[1], Charles A. Geiger[2], and Gerold Tippelt[2]

[1]Department of Geological and Environmental Sciences, Stanford University, Stanford, California 94305-2115, U.S.A.

[2] Department of Materials Science and Physics, Section Mineralogy, Salzburg University, Hellbrunnerstrasse 34, A-5020 Salzburg, Austria

*Corresponding author, E-mail: apalke@stanford.edu

#Currently at Gemological Institute of America, Carlsbad, CA 92008

Abstract

A suite of Fe-bearing natural and synthetic grossular-rich [$(Ca,Fe)_3(Al,Fe)_2Si_3O_{12}$] and pyrope-rich [$(Mg,Fe)_3Al_2Si_3O_{12}$] garnets were investigated using ^{27}Al and ^{29}Si MAS NMR and ^{57}Fe Mössbauer spectroscopy. This was done to study the state of cation order-disorder in garnet solid solutions by analyzing paramagnetically shifted resonances in high-resolution NMR spectra. The Mössbauer spectra, along with electron microprobe results, give the concentrations of Fe^{2+} and Fe^{3+} and their site occupancies, even in grossular samples with very low concentrations of Fe. MAS NMR spectra were collected on Fe^{2+}-bearing grossular- and pyrope-rich garnets with up to 25 mol% almandine component and on other Fe^{3+}-bearing grossular samples with up to 9 mol% andradite component. Despite peak broadening and signal loss, structural information was even obtained from garnet with relatively high Fe contents (25% mole percent almandine component). Paramagnetically shifted NMR peaks, related to the presence of Fe^{2+}, were observed in grossular samples and are similar in nature to those reported previously for natural, relatively low-Fe^{2+} pyrope garnets by Stebbins and Kelsey (2009). Additional NMR peaks appear as the concentration of Fe^{2+} increases, reflecting an increase in the average number of neighboring Fe^{2+} cations around AlO_6 and SiO_4 groups. These newly observed peaks hold potential to provide information concerning the presence or absence of short-range ordering in certain Fe-bearing silicate garnets. The effect of Fe^{3+} on the MAS NMR spectra of garnet appears to be less pronounced, because it does not produce any observable paramagnetically shifted resonances.

Keywords: NMR spectroscopy, Mössbauer spectroscopy, pyrope, grossular, almandine, garnet, paramagnetic shifts, short range order

Introduction

Garnet is an important mineral in various petrological, geochemical and geophysical investigations. It occurs in numerous geologic environments throughout Earth's crust and upper mantle and it is stable with increasing pressure into the deeper transition zone. Garnet's crystal chemical formula is given by $^{VIII}X_3{}^{VI}Y_2{}^{IV}Z_3O_{12}$ with its three crystallographically independent cation sites. The common rock-forming silicate garnets, $^{VIII}X_3{}^{VI}Y_2{}^{IV}Si_3O_{12}$, can incorporate a number of different divalent cations at X and trivalent cations at Y. The resulting solid-solution behavior accounts for the rich crystal chemistry of the garnet group and compositions reflect the conditions of formation (Baxter et al. 2013). Indeed, most natural garnets are typically found as multicomponent solid solutions and crystals rarely occur as pure or nearly pure end members such as grossular ($Ca_3Al_2Si_3O_{12}$), pyrope ($Mg_3Al_2Si_3O_{12}$), almandine ($Fe_3Al_2Si_3O_{12}$) and andradite ($Ca_3Fe_2Si_3O_{12}$). It follows that the structural state, including questions of short- and long-range cation order, is important, because it will affect stability and must be considered in any thermodynamic solid-solution model of garnet.

Diffraction investigations have shown that the aluminosilicate solid-solution garnets, $X_3Al_2Si_3O_{12}$ with X = Ca, Fe^{2+}, Mg and Mn^{2+}, both synthetic and natural, possess no long-range cation order as given by their space group *Ia*-3*d* (Armbruster et al. 1992; Merli et al. 1995). There may be rare exceptions. For example Griffen et al. (1992) argued, based on single-crystal X-ray diffraction results, that a garnet of composition $(Fe_{1.88}Ca_{0.75}Mg_{0.24}Mn_{0.10})_{2.97}$ $(Al_{1.96}Fe_{0.03}Ti_{0.01})_{2.00}Si_{3.01}O_{12}$ shows slight cation order at two crystallographically different X sites in space group $I4_1/acd$. The so-called ugrandite garnets, $Ca_3Y_2Si_3O_{12}$, with Y = Al, Fe^{3+}, and Cr^{3+}, on the other hand, appear to show partial long-range ordering of the Y cations in different space group symmetries lower than *Ia*-3*d*, as described by a number of workers (e.g.

59 Takéuchi et al. 1982; Allen and Buseck 1988; Kingma and Downs 1989; Wildner and Andrut
60 2001).

61 The question of the presence or absence of local short-range order of the cations in both
62 types of garnets is not well understood and has received very little experimental study. Short-
63 range order can, of course, occur even in symmetry *Ia*-3*d*, and is not detectable by standard
64 diffraction measurements. Indeed, the number of methods that can be used to address the
65 question of short-range order is very limited, if nonexistent in a practical sense. The NMR
66 experiment would be, in principle, well suited to study short-range order in garnet and this has
67 been done for synthetic compositions, namely $(Mg_{1-x}Ca_x)_3Al_2Si_3O_{12}$. Here, it has been argued,
68 using ^{29}Si MAS NMR measurements, that a slight degree of Mg/Ca short-range order in
69 intermediate compositions is possible (Bosenick et al. 1995; 1999). This proposal is supported by
70 empirical pair potential (Bosenick et al. 2000) and ab intio calculations (Freeman et al. 2006) and
71 combined computational approaches (Vinograd and Sluiter 2006). Unfortunately, nearly all
72 natural garnets contain paramagnetic cations in various concentrations and thus investigations
73 using conventional MAS NMR spectroscopy are restricted. Early NMR work on a natural
74 pyrope-rich and iron-poor garnet from Dora Maira, Italy, showed that even small amounts of
75 Fe^{2+} cause significant broadening of the ^{29}Si resonance (Geiger et al. 1992), thus limiting
76 quantitative spectral interpretation. The presence of paramagnetic transition metals in various
77 other geologic materials led to similar results in early MAS NMR studies (Oldfield et al. 1983;
78 Sherriff and Hartman 1985).

79 However, recent NMR studies have shown that, despite the problems involved with the
80 presence of paramagnetic species (i.e. signal loss, peak broadening), in some favorable cases
81 information can be gleaned from the NMR spectra of transition-metal-bearing silicate (Dajda et

al. 2003; Palke and Stebbins 2011; Bégaudeau et al. 2012; McCarty et al. 2012; McCarty et al. 2014), rare-earth-element-bearing phosphate (Palke et al. 2013), and transition metal oxide/hydroxide minerals (Kim et al. 2008; Nielsen et al. 2008; Kim et al. 2011; Nielsen et al. 2011). In such cases structural information can be obtained by the observation and analysis of distinct paramagnetically shifted peaks that often fall well outside the range of ordinary chemical shifts. In some, probably more limited situations, NMR signal loss, ordinarily seen as a complication caused by the presence of paramagnetic species, has been used to answer questions about short-range order/disorder in geologic materials (Palke et al. 2012). NMR spectroscopy of technologically important paramagnetic inorganic materials (cf. Middlemiss et al. 2013) as well as proteins and other organic compounds (cf. Bertini et al. 2005) are flourishing areas of research. NMR spectroscopic study of paramagnetic species has yet to be widely applied to geologically important minerals.

In this paper we report the results of a ^{27}Al and ^{29}Si MAS NMR and ^{57}Fe Mössbauer spectroscopy study of a suite of natural and synthetic Fe-bearing grossular- and pyrope-rich garnets. While Fe^{3+} is largely absent from pyrope-rich garnets, in grossular-rich garnets both Fe^{2+} and Fe^{3+} can be found at the X- and Y-sites, respectively. High-resolution NMR spectra can be collected to identify important structural components, such as the likely presence of tetrahedral Al in certain synthetic garnets and paramagnetically shifted resonances, as already documented in natural low Fe^{2+} pyrope-rich garnets (Stebbins and Kelsey 2009; Palke and Stebbins 2011). Despite peak broadening at higher concentrations of Fe^{2+} (up to 25 mol% Fe^{2+} replacing either Mg or Ca), individual peaks can still be resolved and assigned to specific local structural configurations around SiO_4 or AlO_6 groups having various numbers of nearby Fe^{2+} neighbors. Careful analysis of the intensities of these features in the NMR spectra of compositionally

105 homogeneous Fe^{2+}-bearing garnets could provide information on the question of short-range
106 ordering in pyrope- and grossular-rich garnets.
107
108 **Experimental**
109 **Natural and synthetic garnet samples**
110 **Table 1** lists the geographical localities of the natural garnets and literature references for
111 both natural and synthetic samples studied herein. In the absence of literature citations,
112 established labels for samples that came from the research collection of one of the authors
113 (CAG) are reported in case they are used in future studies. Sample labels are also provided for
114 those from the Stanford Research Mineral Collection – #50790 (sample G10 in **Table 1**) and
115 #64758 (not included in **Table 1** because no spectra are presented – however this sample is
116 discussed below). However, considering the large number of garnets from various sources, a new
117 labeling scheme was employed. Grossular-rich samples are labeled G1 through G12, in order of
118 increasing Fe concentration. Pyrope-rich samples are likewise labeled as P1 through P6. In most
119 instances the label is followed by a simple compositional description in terms of the mole
120 percent of the garnet end members. For instance, sample G1, composed of a 99.5 mol% grossular
121 and a 0.5 mol% andradite component, is referred to as G1-$Grs_{99.5}And_{0.5}$. The pyrope component
122 of grossular-rich samples is usually less than 2-3 % and was ignored and vice versa for the
123 grossular component in pyrope garnets. Therefore, the grossular samples are described using
124 compositions normalized to the following three components: grossular (Grs – $Ca_3Al_2Si_3O_{12}$),
125 andradite (And – $Ca_3Fe_2Si_3O_{12}$), and almandine (Alm – $Fe_3Al_2Si_3O_{12}$). Pyrope garnets are
126 reported in terms of the pryope (Prp – $Mg_3Al_2Si_3O_{12}$) and almandine components. Abbreviations
127 for garnet end members are taken from Whitney and Evans (2010).

The synthesis of several garnets (i.e., G11, G12, P3 and P6, **Table 1**) is described in Geiger et al. (1987). The synthesis of one sample for this work (G8, **Table 1**) followed closely the procedure outlined in Armbruster and Geiger (1993). That for another synthetic garnet (G7, **Table 1**) attempted to closely follow the procedure of Geiger et al. (1987), replacing the step in which the starting materials are melted in a graphite crucible with melting in air in a platinum crucible. The synthetic garnets G11, G12, P3 and P6 have been well characterized (Geiger et al. 1987). In many, but not all, cases this includes powder IR spectroscopy (Geiger 1998; Boffa Ballaran et al. 1999), ^{57}Fe Mössbauer spectroscopy (Geiger et al. 2003), and X-ray powder diffraction and electron probe microanalysis (Geiger and Feenstra 1997).

X-ray powder diffraction

Powder XRD was performed for selected samples on a Rigaku Geigerflex X-ray diffractometer and data were compared to those published by the International Centre for Diffraction Data. In general, XRD peaks could be indexed to pyrope- or grossular-rich garnet with no indication of minor "impurity" phases. Full structure refinements were not performed and the interatomic distances cited below for pyrope-almandine and grossular-almandine-andradite garnets are assumed to be similar to those for the dominant end member (pyrope or grossular). References to previously published XRD data can be found in **Table 1**.

Electron probe microanalysis

The compositions of all samples were analyzed using Electron Probe MicroAnalysis (EPMA) on either the JEOL 733 at Stanford University or the Cameca SX-100 at the University of California, Davis, using various natural or synthetic materials for intensity standards. Data for

151 several samples were collected in both labs and were in good agreement. Relative uncertainties
152 in the EPMA data are 1.5 % or less for major elements (Al, Si, either Mg or Ca, and sometimes
153 Fe) and 15 to 25 % for minor elements (Mn, Ti, sometimes Fe, and either Ca or Mg). EPMA data
154 were reduced to garnet crystal chemical formulae ($^{VIII}X_3{}^{VI}Y_2{}^{IV}Z_3O_{12}$) by assigning Si and Ti to
155 the tetrahedral Z site, Al and Fe^{3+} to the octahedral Y site, and Mg, Ca, Mn, and Fe^{2+} to the
156 dodecahedral X site (**Table 1**). Relative amounts of Fe^{2+} and Fe^{3+} were determined by
157 Mössbauer spectroscopy as described below. While it may be controversial to relegate Ti to the
158 tetrahedral Z site, this element is present in such small amounts that the actual site preference of
159 Ti in these garnets is inconsequential for this study.
160
161 **^{57}Fe Mössbauer spectroscopy**
162 Spectra were recorded using the standard set-up of the Salzburg Mössbauer lab (e.g.
163 Redhammer et al. 2005), which is outlined just in short form here. Transmission powder spectra
164 were recorded at 293 K using a conventional spectrometer in horizontal arrangement (^{57}Co/Rh
165 single line thin source, 50 mCi initial activity, constant acceleration mode with a symmetric
166 triangular velocity shape, multi-channel analyzer with 1024 channels, velocity range ± 4 mm/s).
167 Powdered garnet was held between plastic discs fitted into a Cu-ring of 10 mm inner diameter
168 covered with Al-foil on one side. The two symmetric spectra (512 channels each) were folded,
169 calibrated against α-iron and evaluated using the fit program RECOIL.
170
171 **^{29}Si and ^{27}Al NMR MAS spectroscopy**
172 ^{29}Si MAS NMR spectra were collected either with a Varian Infinity-Plus 400
173 spectrometer at 9.4 T (79.5 MHz) or a Varian Unity/Inova 600 spectrometer at 14.1 T (119.1

MHz) using Varian/Chemagnetics "T3"-type probes and 3.2 mm ZrO_2 rotors spinning up to 23 kHz. External TMS was used as a frequency reference. For low concentration Fe-containing samples, ^{29}Si spectra were collected with a single pulse sequence using carefully calibrated 30° tip angles. It proved difficult to collect spectra with a smooth baseline for garnets with higher concentrations of Fe because of rapid signal decay. Thus, for these samples (G12, P4, P5, and P6, **Table 1**) ^{29}Si spectra were collected at a field of 9.4 T using a spin-echo pulse sequence (90-τ-180) with a minimal echo delay of one rotor period and a pulse delay of 0.1 s. These spectra were fully relaxed using this short pulse delay due to the larger amount of Fe present. However, samples with less Fe (~1 wt.% FeO or less) were not fully relaxed using a pulse delay of 0.1 s, even using a smaller tip angle of 30°. The ^{29}Si spectra shown in this work were collected either with single pulse or spin echo sequences and pulse delays of 0.1 s in order to emphasize paramagnetically shifted peaks. However, in some cases pulse delays of up to 600 s were used in combination with spectra collected with short pulse delays of 0.1 s to get accurate peak area measurements on fully relaxed spectra.

^{27}Al MAS NMR spectra were collected at three fields from the Infinity-Plus 400 spectrometer at 9.4 T (104.1 MHz) to the Varian Unity/Inova 600 spectrometer at 14.1 T (156.3 MHz) to the Varian Unity/Inova spectrometer at 18.8 T (208.3 MHz). In all cases a Varian/Chemagnetics "T3" probe was used with 3.2 mm ZrO_2 rotors at spinning speeds up to 22 kHz. External 0.1 M aqueous $Al(NO_3)_3$ solution was used as a frequency reference. Pulse delays of 0.1 s gave fully relaxed spectra and maximized signal to noise in most cases, but a few samples with low Fe concentrations (<1 wt.% FeO) required pulse delays of up to 10 s to collect fully relaxed spectra.

Estimated uncertainties for NMR peak integrals were determined by fitting spectra from multiple single-pulse spectra collected at varying spinning speeds, pulse delays, and/or magnetic fields for certain samples. In general, uncertainties in peak integrals are estimated to be ±5-10 % absolute intensity for each peak. Other estimated uncertainties in the NMR spectra reported here are typically ± 0.5 ppm for peak position and ± 5 % of full width at half maximum (FWHM). When observed, spinning sidebands corresponding to the central transitions were included in relative peak areas; when needed for peaks with large paramagnetic shifts, central resonances were distinguished from spinning sidebands by varying the spinning speed.

Results and Discussion

^{57}Fe Mössbauer and EPMA results

All natural grossular-rich samples were analyzed by Mössbauer spectroscopy to determine their $Fe^{2+}/(Fe^{2+} + Fe^{3+}) = Fe^{2+}/Fe_{total}$ ratios and to assign Fe^{2+} and Fe^{3+} to the X or Y site of garnet. This is necessary in order to separate the distinct contributions from either Fe^{2+} or Fe^{3+} to the various features of the ^{27}Al and ^{29}Si NMR spectra. Fe^{2+}/Fe_{total} was determined from simple two doublet fits to the various spectra (one Fe^{2+} and one Fe^{3+} doublet) as shown in **Figure 1**. The doublet assignments for Fe in common silicate garnet are known well (Amthauer et al. 1976) and the minor effect of anisotropic recoil free fraction on the exact shape of the Fe^{2+} doublet (Geiger et al. 1992; Geiger et al. 2003) was not considered. The recoil free fractions for Fe^{2+} and Fe^{3+} are considered to be the same. The determination of Fe^{2+}/Fe_{total} in the natural samples was challenging due to the low concentration of Fe and the low natural abundance of ^{57}Fe, as shown in the fair to poor signal to background ratios of some spectra. However, through the long counting times employed, Fe^{2+}/Fe_{total} could be measured for most samples with

219 reasonable accuracy (**Table 1**). Mössbauer spectra were also collected for two synthetic ^{57}Fe-
220 enriched grossular-rich garnets, G7 and G8. Data for these samples were analyzed as for the
221 natural samples and their Fe^{2+}/Fe_{total} ratios are reported in **Table 1**. No interpretable Mössbauer
222 spectrum could be collected for G1; however, we assume that most of the iron in this sample
223 exists as Fe^{3+} based on the absence of any paramagnetically shifted ^{29}Si NMR peaks related to
224 Fe^{2+}, as described below. However, given the low concentration of Fe in this sample, it would be
225 difficult to ascertain the oxidation state with either Mössbauer or ^{29}Si NMR.
226 Measurements of Fe^{2+}/Fe_{total} were used in conjunction with EPMA data in order to
227 determine the stoichiometric garnet compositions for the samples studied here and the results are
228 reported in **Table 1**. The synthetic samples in this study were generally found to be somewhat
229 compositionally heterogeneous. This is especially true for samples G11 and P3 and to a lesser
230 extent G12 and P6. Compositional heterogeneity is usually manifested as small domains (~1-10
231 μm) of relatively almandine-rich crystals that were observed using backscattered electron
232 imaging on the electron microprobe. When the almandine-rich data points are not considered for
233 samples G12 and P6, the result is a fairly homogeneous composition approaching the intended
234 bulk composition for these samples (25 mole % almandine and 75 mole % grossular or pyrope).
235 Given the low abundance of these almandine-rich domains in G12 and P6 (less than a few %),
236 compositions are reported based on the corrected data set as just described (**Table 1**). G11 and
237 P3 were more compositionally heterogeneous. We therefore report the intended bulk
238 compositions for these two samples in **Table 1**. The natural pyrope-rich samples P4 and P5 are
239 broken sand- to small gravel-sized fragments taken from larger crystals from two separate
240 localities at the Dora Maira, Italy ultra-high pressure locality. While individual grains can be
241 compositionally homogeneous, the proportions of pyrope and almandine vary significantly from

grain to grain. Compositions for P4 and P5 therefore are averages of 10 to 20 analyses of various grains from samples that came directly out of the NMR rotor after collection of their spectra.

Garnet crystal structure

In order to better understand the NMR results and the various possible local X cation configurations, we discuss briefly the garnet structure, as reviewed by Geiger (2013). The cubic structure, space group *Ia-3d*, consists of strongly bonded ZO_4 tetrahedra and YO_6 octahedra that share corners, giving rise to a quasi three-dimensional framework. The more weakly bonded X cations are coordinated by 8 oxygen atoms in the form of a triangular dodecahedron. Local relationships among the three coordination polyhedra relevant to this work are shown in **Figures 2a-c**, which illustrate the first and/or second X-site neighbors to Si and Al and the bond pathways that connect them. These structural relationships are important for assigning paramagnetically shifted NMR peaks to specific local configurations (see below).

^{27}Al NMR spectroscopy

Paramagnetically shifted NMR peaks and local Fe^{2+}-Al configurations. The ^{27}Al NMR spectra of three pyrope-rich garnets, P2-$Prp_{93.3}Alm_{6.7}$, P4-$Prp_{88.0}Alm_{12.0}$, and P5-$Prp_{83.2}Alm_{16.8}$, are shown in **Figure 3**. ^{27}Al NMR spectra for sample P2-$Prp_{93.3}Alm_{6.7}$ were reported previously by Stebbins and Kelsey (2009) and Palke and Stebbins (2011). Two paramagnetically shifted NMR resonances, labeled A1 and A2 occurring at +33.6 and +66.0 ppm, respectively, were observed in addition to the main, "unshifted" peak at +1.1 ppm corresponding to that of end-member pyrope (^{27}Al surrounded by only Mg in nearest neighboring dodecahedra), labeled as A0 in **Figure 3**. This is in close agreement with the value

265 of the isotropic chemical shift of +2.9 ppm as measured by Kelsey et al. (2007). The same
266 features are seen in the spectra of P4-$Prp_{88.0}Alm_{12.0}$ and P5-$Prp_{83.2}Alm_{16.8}$ in addition to a new,
267 low intensity feature seen at +94.0 ppm (labeled A3 in **Figure 3**) for P5-$Prp_{83.2}Alm_{16.8}$. The Al
268 cations in AlO_6 octahedra in almandine/pyrope garnets have 6 crystallographically identical X-
269 site nearest neighbors at a distance of about 3.201 Å (Armbruster et al. 1992) that can be
270 occupied by either Mg or Fe^{2+}. Palke and Stebbins (2011) assigned the A0, A1, and A2
271 resonances to AlO_6 groups with 0, 1, or 2 Fe^{2+} cations in one of these six neighboring X-sites
272 (**Figure 2a**), respectively. These assignments were made considering the higher intensity of A1
273 compared to A2 and the increasing intensity of both these peaks with increasing Fe^{2+}
274 concentration. This proposal is further bolstered by the fact that A2 is shifted in frequency twice
275 as far from A0 as A1. The presence of A3 in only the pyrope with the highest Fe^{2+} concentration,
276 along with its frequency shift from A0 that is roughly three times larger than that for A1,
277 indicates that this resonance can be assigned to AlO_6 octahedra having three Fe^{2+} neighbors in
278 the first shell of X-sites (**Figure 2a**). It follows that at slightly higher concentrations of Fe^{2+} one
279 would expect to observe a fifth resonance A4 at approximately +120 ppm. In fact, in a single
280 crystal ^{27}Al NMR study of an almandine garnet with composition Prp22Alm78, Brinkmann and
281 Kaeser (1972) described discrete resonances for AlO_6 groups having 4, 5, and 6 Fe^{2+} neighbors.
282 They used the relative intensities of these peaks to determine the almandine component by
283 measuring the amount of Fe^{2+} occupying the garnet X-site. A rigorous comparison of Fe^{2+}
284 content and site populations in our study was not attempted because of the compositional
285 heterogeneity of P4-$Prp_{88.0}Alm_{12.0}$, and P5-$Prp_{83.2}Alm_{16.8}$. However, with compositionally
286 homogeneous pyrope-almandine garnets it could be possible to investigate the state of cation
287 order-disorder at the X-site.

In general, the ^{27}Al NMR spectra of the Fe-bearing grossular samples are characterized by the presence of a single peak around -6 ppm when measured at a field of 14.1 T, in close agreement with the previously measured isotropic chemical shift of -3.5 ppm (Kelsey et al. 2007). Only one relatively low Fe sample (G4-$Grs_{98.9}Alm_{0.5}And_{0.6}$) showed the characteristic quadrupolar splitting expected for end-member grossular (Kelsey et al. 2007). For the most part, ^{27}Al NMR peak widths (full width at half maximum = FWHM) increase with increasing Fe_{total} + Mn content (**Figure 4a**). However, there is no monotonic increase in peak width with increasing Fe_{total} + Mn from sample to sample. This is likely due to the variable influence of Fe^{2+}, Fe^{3+}, and Mn^{2+} on NMR relaxation rates and the difference in the relative proportions of these cations in the garnets of this study (**Table 1**). A similar relationship is observed for ^{29}Si NMR peak widths as a function of Fe_{total} + Mn content (**Figure 4b**). The ^{27}Al NMR spectra of the grossular-rich garnets G7-$Grs_{96.9}Alm_{1.5}And_{1.6}$, G9-$Grs_{96.7}Alm_{2.9}And_{0.4}$, G10-$Grs_{91.2}And_{8.8}$, G11-$Grs_{90.0}Alm_{10.0}$, and G12-$Grs_{75.2}Alm_{24.8}$ are shown in **Figure 5**. The spectrum of G11-$Grs_{90.0}Alm_{10.0}$ shows three distinct peaks, one main, intense peak at -5.1 ppm, one smaller resonance at +15.8 ppm, and a minor, low intensity peak at +59.3 ppm. The relative intensity of the feature at +15.8 ppm and the magnitude of its frequency shift from the main peak is similar to that of peak A1 observed in the spectra of pyrope-almandine garnets. We assign this feature in G11-$Grs_{90.0}Alm_{10.0}$ to a local configuration with an AlO_6 octahedron with one Fe^{2+} cation in a nearest neighboring X-site (**Figure 2a**), as for the pyrope garnets above. The smaller frequency shift of A1 from A0 in grossular-almandine (+21.9 ppm) vs. pyrope-almandine (+32.5 ppm) garnets is reasonable given the longer distance between Al and the X-site cation of 3.309 Å in grossular (Geiger and Armbruster 1997) vs. 3.201 Å in pyrope (Armbruster et al. 1992). Peak A1 is probably also present as a low intensity shoulder on the main peak in the spectrum of G9-$Grs_{96.7}Alm_{2.9}And_{0.4}$,

311 although this is not readily apparent in **Figure 5**. The ^{27}Al NMR spectrum of the grossular
312 sample with the highest almandine component (G12-$Grs_{75.2}Alm_{24.8}$) shows a very broad peak (ca.
313 80 ppm FWHM) centered at +12.1 ppm. There may also be a minor contribution from a narrower
314 resonance (ca. 30 ppm FWHM) located at -5.7 ppm. Although peak broadening is too large to
315 resolve contributions from individual resonances, the shift in the center of gravity by nearly + 20
316 ppm and the 80 ppm line width are almost certainly caused by the presence and overlap of
317 multiple, unresolvable peaks corresponding to AlO_6 groups having 0, 1, 2, 3, and 4 next nearest
318 Fe^{2+} neighbors at X-sites (i.e. peaks A0, A1, A2, A3, and A4). However, neither peak A1 nor
319 any other paramagnetically shifted peaks are seen in the spectra of the other grossular-rich
320 samples. This is due to their lower Fe^{2+} concentrations and their generally broader peaks
321 compared to the pyrope-rich garnets – e.g. 15 ppm vs. 9 ppm FWHM for peak A0 for grossular
322 and pyrope samples having similar almandine components, G11-$Grs_{90}Al_{10}$ and P3-$Prp_{90}Al_{10}$,
323 respectively, **Table 2**.
324
325 **Tetrahedrally Coordinated Al in Garnet.** A low intensity resonance is observed at
326 +59.3 ppm in the ^{27}Al NMR spectrum of G11-$Grs_{90.0}Alm_{10.0}$. One possible interpretation assigns
327 it to an AlO_6 group with two Fe^{2+} cations in nearest neighbor X-sites, analogous to resonance A2
328 in the spectra of pyrope-rich garnets. However, this peak at +59.3 ppm in G11-$Grs_{90.0}Alm_{10.0}$ is
329 located at a position more than twice the frequency shift of peak A1, which should lead to an A2
330 resonance at +37.7 ppm.
331 Alternatively, this resonance at +59.3 ppm could be assigned to Al at the tetrahedral site
332 of this garnet. Similar peaks are observed at +59.7 ppm in the ^{27}Al NMR spectra of sample G7-
333 $Grs_{96.9}Alm_{1.5}And_{1.6}$ (**Figure 5**) and G8-$Grs_{95.5}And_{4.5}$ (not shown). The presence of this resonance

in the spectra of grossular-rich garnets with only Fe^{2+} or only Fe^{3+} indicates it is not a paramagnetically shifted Al peak. Thus, it is assigned to AlO_4 groups. Tetrahedrally coordinated Al is known to occur in certain uncommon silicate garnets such as kimzeyite, $^{VIII}Ca_3{}^{VI}Zr_2{}^{IV}Al_2{}^{IV}SiO_{12}$ (Schingaro et al. 2001) or hutcheonite, $^{VIII}Ca_3{}^{VI}Ti_2{}^{IV}Al_2{}^{IV}SiO_{12}$ (Ma and Krot 2014), but as far as we know, it has never been documented experimentally for common aluminosilicate garnets. Tetrahedrally coordinated Al has been proposed, in some cases, based on indirect arguments using chemical data in order to maintain stoichiometric garnet composition (cf. Huggins et al. 1977; Deer et al. 1992). Another possibility is that the tetrahedrally coordinated Al might reflect a minor "impurity" phase in the garnet. However, as noted above, these samples have been characterized for phase purity using XRD, EPMA, and ^{27}Al and ^{29}Si NMR spectroscopy. The only indication of an "impurity" phase comes from EPMA mapping of sample G7-$Grs_{96.9}Alm_{1.5}And_{1.6}$ in which a few small grains (~1-5 μm) were observed as bright spots in backscattered electron images. One of these was large enough to obtain two EPMA measurements identifying them as a wollastonite-like phase ($CaSiO_3$). However, only a small amount of Al was measured here, corresponding to 0.001 to 0.076 atoms of Al per formula unit. This is insufficient to explain the presence of 5-10% tetrahedrally coordinated Al in the ^{27}Al NMR spectra of G7-$Grs_{96.9}Alm_{1.5}And_{1.6}$, G8-$Grs_{95.5}And_{4.5}$ and G11-$Grs_{90.0}Alm_{10.0}$. All this strongly suggests that synthetic grossular samples can contain small amounts of tetrahedrally coordinated Al. The possibility for the occurrence of tetrahedrally coordinated Al in aluminosilicate garnet was also suggested in the ^{27}Al NMR spectra of synthetic Sc-bearing pyrope and grossular (Kim et al. 2007).

The charge-balancing substitution mechanism by which Al^{3+} could substitute for Si^{4+} is, as yet, unknown. One could suggest the concomitant substitution of dodecahedrally coordinated

357 Fe^{3+} (0.78 Å, Shannon 1976) for Ca^{2+} (1.12 Å, Shannon 1976) to allow for some tetrahedrally
358 coordinated Al^{3+}, but Fe^{3+} is probably too small to reside at the X-site of garnet. We also did not
359 observe any octahedrally coordinated Si in the ^{29}Si NMR MAS spectra of these garnets, thus
360 eliminating a mechanism of Al-Si disorder over the tetrahedral and octahedral sites. It may also
361 be possible that tetrahedrally coordinated Al could be present as a defect at an interstitial site
362 (Geiger et al. 2013). Finally, it should be noted that this tetrahedrally coordinated Al is present
363 only in synthetic garnet crystallized at high temperature and rapidly quenched. There is no
364 evidence for tetrahedrally coordinated Al in the natural grossulars studied here, most of which
365 formed in Ca-rich mineralized pods in serpentinites (i.e. rodingites) at relatively low
366 temperatures of ~200-300°C (Normand and Williams-Jones 2007; Bach and Klein 2009). It is
367 possible, then, that the tetrahedrally coordinated Al only occurs in high temperature synthetic
368 garnets.
369
370 **^{29}Si NMR spectroscopy**
371 **Paramagnetically shifted NMR peaks and local Fe^{2+}-Si configurations.** The ^{29}Si
372 NMR spectrum of G7-$Grs_{96.9}Alm_{1.5}And_{1.6}$ is shown in **Figures 6a-b** along with that for P1-
373 $Prp_{97.3}Alm_{2.7}$ from Stebbins and Kelsey (2009) and Palke and Stebbins (2011) for comparison.
374 The spectra of both samples share the same fundamental features with a main peak at -83.3 ppm
375 for G7 and -71.9 ppm for P1 and two lower intensity peaks shifted to lower frequency at -94.0
376 ppm (S1) and -101.4 ppm (S2) for G7 and -79.8 ppm (S1) and -88.1 ppm (S2) for P1 (**Figure**
377 **6a**). For G7-$Grs_{96.9}Alm_{1.5}And_{1.6}$ it was necessary to use a lower-field spectrometer (9.4 T) and
378 3.2 mm rotors spinning at 23 kHz in order to locate peak S4, found in previous studies of Dora
379 Maira pyropes (Stebbins and Kelsey 2009; Palke and Stebbins 2011), which has a large positive

380 frequency shift (+103 ppm for G7 vs. +134 ppm for P1, **Figure 6b**). The position of the main
381 peaks for G7 and P1 agree with those measured for pure endmember grossular and pyrope at -
382 83.4 (Janes et al. 1985) and -72.0 ppm (Phillips et al. 1992), respectively. This provides the
383 assignment of these peaks to SiO_4 groups with zero nearby Fe^{2+} neighbors (i.e. within ~6 Å). In
384 the spectra of both G7-$Grs_{96.9}Alm_{1.5}And_{1.6}$ and P1-$Prp_{97.3}Alm_{2.7}$ peaks S1 and S2 have nearly
385 equal integrated intensities, while S4 has half the intensity of either S1 or S2. This agrees well
386 with the peak assignment scheme proposed by Palke and Stebbins (2011), wherein S4 is assigned
387 to a local configuration where Fe^{2+} occupies one of the two edge-shared dodecahedral X-sites
388 linked to a SiO_4 tetrahedron with a Si-X distance of 2.863 Å in pyrope (Armbruster et al. 1992)
389 and a Si-X distance of 2.959 Å in grossular (Geiger and Armbruster 1997) – see **Figure 2b**. Peak
390 S2 is assigned to a configuration with Fe^{2+} at one of the four corner-shared dodecahedral X sites
391 with a Si-X distance of 3.506 Å in pyrope (Armbruster et al. 1992) and a Si-X distance of 3.624
392 Å in grossular (Geiger and Armbruster 1997) – see **Figure 2b**. Based on the above analysis
393 whereby the peaks S2 and S4 are assigned to local configurations with edge- and corner-shared
394 dodecahedra to the SiO_4 tetrahedron, only peak S1 is left unassigned. Therefore, we must also
395 consider local configurations with dodecahedral sites that are four bonds away from Si (e.g. Si-
396 O-Al-O-X, X = Mg, Ca, Fe^{2+}). This gives 12 more dodecahedral sites that are split into three
397 symmetrically inequivalent groups of four dodecahedral X-sites with Si-X distances of 5.356,
398 5.356, and 5.726 Å for pyrope (Armbruster et al. 1992) and Si-X distances of 5.536, 5.536, and
399 5.918 Å for grossular (Geiger and Armbruster 1997). These local configurations are shown in
400 **Figure 2c**. The presence of Fe^{2+} in these sites should produce three more paramagnetically
401 shifted ^{29}Si peaks. The fact that only S1 is observed, indicates that occupation of only one of
402 these dodecahedral sites by Fe^{2+} produces a significant frequency shift for the ^{29}Si nucleus. Peaks

403 arising from Fe^{2+} at the other two X-sites may have frequency shifts that are too small to be
404 observed. The existence of four dodecahedra at which Fe^{2+} can be located to produce either S1 or
405 S2 and only two for S4 explains the 1:2 ratio of peak intensities of S4 to either S1 or S2.
406 The ^{29}Si NMR spectrum of Fe^{3+}-bearing, Fe^{2+}-free garnet G8-$Grs_{95.5}And_{4.5}$ is also shown
407 in **Figure 6a**. No paramagnetically shifted ^{29}Si peaks are observed, as is also the case for the
408 other Fe^{2+}-free garnet G10-$Grs_{91.2}And_{8.8}$. The spectra for these samples are characterized by a
409 single resonance having an unusual lineshape, which, due to its relatively broad base, cannot be
410 adequately fit using a single Lorentzian or Gaussian peak or a combination of the two. A
411 minimum of two Lorentzian components was needed to sufficiently model the resonances in
412 these spectra. In the best fit of the spectra, the relative contributions of the narrow and broad
413 components are similar with the broad component comprising 62 and 67% of the total signal for
414 G8-$Grs_{95.5}And_{4.5}$ and G10-$Grs_{91.2}And_{8.8}$, respectively. The lack of a significant increase in the
415 intensity of the broad component as the ferric iron content increases indicates that this unusual
416 lineshape is not related directly to the presence of paramagnetically shifted peaks as seen in the
417 ^{29}Si and ^{27}Al NMR spectra of ferrous-iron-bearing pyrope garnets and other minerals (Stebbins
418 and Kelsey 2009, Palke and Stebbins 2011, McCarty et al. 2012, Bégaudeau et al. 2012). The
419 likely explanation is that the two-component fit to this resonance in the ^{29}Si NMR spectra is
420 simply a useful approximation to describe a single resonance with an unusual lineshape, neither
421 completely Gaussian nor Lorentzian, related to the poorly understood effect of ferric iron on the
422 nuclear spin relaxation of ^{29}Si in these materials.
423 Most of the grossular-rich garnets in this study are solid solutions consisting of grossular,
424 almandine, and andradite components. Their ^{29}Si NMR spectra should, in principle, contain
425 features characteristic of both grossular-almandine and grossular-andradite solid solutions.

426 **Figure 7** shows the ^{29}Si NMR spectrum of synthetic grossular G7-$Grs_{96.9}Alm_{1.5}And_{1.6}$ along with
427 the individual components used in fitting the spectrum. Paramagnetically shifted peaks S1 and
428 S2 are present due to the presence of Fe^{2+}. However, a fit consisting only of the main unshifted
429 resonance and peaks S1 and S2 does not provide an accurate description of the measured
430 spectrum. The addition of a broad component underlying the main unshifted peak ("USB" in
431 **Figure 7**), as described for the Fe^{3+}-rich garnets above, significantly increases the quality of the
432 fit. Using the fits shown in **Figure 7,** peaks S1 and S2 have relative intensities of 5.5 % and 4.9
433 %, respectively. Assuming a statistically random distribution of Fe^{2+} over the X sites in garnet,
434 we can calculate the intensities of peaks S1 and S2 from the equation, $I = mx^k (1-x)^{n-k}$. Here "m"
435 is the number of local configurations that can give rise to a specific peak (equal to 2 for peak S4
436 and 4 for S1 and S2), "x" is the probability of Fe^{2+} occupying an X-site (the almandine
437 component from **Table 1**), "k" is the number of Fe^{2+} cations interacting with the ^{29}Si nucleus
438 giving rise to the peak in question, and "n" is the total number of sites at which Fe^{2+} can be
439 located to create a paramagnetically shifted peak (i.e. equal to 10 here for the 2, 4, and 4 sites
440 related to peaks S4, S1, and S2). Instead of calculating the intensities of peaks S1 and S2, one
441 could alternatively measure the concentration of Fe^{2+} using their observed intensities. Most of
442 the grossular samples studied here show peaks S1 and S2 in their ^{29}Si NMR spectra and the
443 concentrations of Fe^{2+} obtained from the measurement of their intensities are reported in **Table**
444 **2**. The ^{29}Si MAS NMR parameters obtained from fitting the spectra for these samples are
445 provided in the **Supplementary Table S1**. Concentrations obtained in this way agree well with
446 those measured by a combination of EPMA and Mössbauer spectroscopy (**Table 2**). The good
447 agreement between our NMR data and EPMA (+ Mössbauer) results suggests that the intensities

448 of paramagnetically shifted peaks can provide reliable and quantitative determinations of Fe^{2+} in
449 Fe-bearing silicates.
450
451 **Relevance to X-cation short-range order-disorder.** One of the main goals of this
452 investigation is to address the state of cation order-disorder in Fe-bearing pyrope- and grossular-
453 rich garnet solid solutions. The ^{29}Si spectra of the four garnets with the highest Fe concentration
454 in this study, P4-$Prp_{88.0}Alm_{12.0}$, P5-$Prp_{83.2}Alm_{16.8}$, P6-$Prp_{73.7}Alm_{26.3}$, and G12-$Grs_{75.2}Alm_{24.8}$, are
455 shown in **Figures 8a-b and 9**. Peaks S1 and S2 are observed in addition to the main unshifted
456 peak for P4-$Prp_{88.0}Alm_{12.0}$. However, because of increased peak broadening at higher
457 concentrations of Fe^{2+}, it is impossible to resolve individual peaks in this central region of the
458 spectra. For garnets P5-$Prp_{83.2}Alm_{16.8}$, P6-$Prp_{73.7}Alm_{26.3}$, and G12-$Grs_{75.2}Alm_{24.8}$, the main
459 unshifted peak and peaks S1 and S2 merge into a single broad, asymmetric band of resonances
460 with a center of gravity that shifts to progressively lower frequency with increasing Fe^{2+}
461 (**Figures 8a-b**). The loss of resolution in this band of resonances can also be attributed, in part, to
462 the presence of peaks related to SiO_4 tetrahedra having two or more nearby Fe^{2+} neighbors in
463 configurations related to peaks S1 and S2 (corner-shared sites or second cation neighbors). In
464 other words, at higher concentrations of Fe^{2+}, peaks consisting of combinations of S1 and S2,
465 such as S2+S2, S1+S2+S2, S1+S1+S1, etc., will have non-negligible intensities. The overlap of
466 all these peaks leads to asymmetric, heterogeneous line broadening in addition to the
467 homogeneous broadening caused by the relaxation effects of paramagnetic Fe^{2+}.
468 Despite the loss of resolution between peaks S1, S2, and the unshifted peak at high Fe^{2+}
469 concentration, resonances with larger paramagnetic shifts (e.g. S4) can still be observed, which
470 correspond to SiO_4 groups having Fe^{2+} in adjacent edge-shared X-sites. They can, thus, provide

information of the state of order-disorder of Fe^{2+} at the X-sites in pyrope- and grossular-rich garnets. The peaks centered at about -70 to -90 ppm have only Mg^{2+} or Ca^{2+} in adjacent edge-shared dodecahedral X-sites, while S4 at about +100 to +130 ppm has one Fe^{2+} and either Mg^{2+} or Ca^{2+} in adjacent edge-shared X-sites. In the four garnets with the largest almandine contents, an additional low intensity resonance is observed at about +310 and +330 ppm for grossular- and pyrope-rich compositions, respectively (**Figure 9**). This peak is only observed in spectra collected at a low magnetic field (9.4 T), where high spinning speeds of 23 kHz were sufficient to separate spinning sidebands from the isotropic resonances. This feature is shifted by about +400 ppm from the pure pyrope or grossular peaks, at about -70 or -80 ppm, respectively, while peak S4 is shifted by about +200 ppm. The fact that the paramagnetic shift of this new feature is twice that of S4, along with its low intensity (about 5-15 % of the total), argues for its assignment to SiO_4 tetrahedra having Fe^{2+} in both adjacent edge-shared X-sites. We hereafter refer to this peak as S4+S4.

Because there is some compositional heterogeneity and/or zoning in these four garnets, it is difficult to determine their precise structural state (i.e., if, for example, short-range cation order is present). We note that the presence of the S4+S4 resonance indicates that a local configuration with Fe^{2+} cations in the two dodecahedra sharing polyhedral edges with a common SiO_4 tetrahedron can occur in grossular- and pyrope-rich garnets. The computational studies have shown that in grossular-rich compositions that it is energetically unfavorable to have Mg cations in the two dodecahedra sharing polyhedral edges, and vice versa with respect to Ca cations in pyrope-rich garnets (Bosenick et al. 2000; Freeman et al. 2006). Given the similarity in ionic radii between $^{VIII}Mg^{2+}$ (0.89 Å) and $^{VIII}Fe^{2+}$ (0.92 Å), one might expect that the local configuration reflected by the S4+S4 peak will also be energetically unfavorable in grossular-

494 rich garnets. Further NMR studies using demonstrably homogeneous samples are needed to
495 clarify the question of order/disorder in pyrope- and grossular-rich garnets. Future work might
496 also focus on the effect that synthesis/formation temperature will have on the potential short-
497 range order that might be observable using NMR spectroscopy.

498 It should be expected that if any short-range X-site cation order is present in garnet solid
499 solutions, that it would be more readily detectable in intermediate compositions. However, the
500 problems associated with paramagnetic interactions become more severe with increasing
501 concentrations of the paramagnetic species. The NMR spectra are, then, difficult, if not
502 impossible, to interpret. There are few published MAS NMR studies of silicate minerals with
503 higher concentrations of transition metals than the Dora Maira pyrope garnet with a 6.7 mol%
504 almandine component (P1-$Prp_{93.3}Alm_{6.7}$, **Table 1**) reported previously (Stebbins and Kelsey
505 2009; Palke and Stebbins 2011). In order to test the limits of our methodology, we measured the
506 ^{27}Al and ^{29}Si MAS-NMR spectra of a natural, Fe-rich garnet (Stanford Research Mineral
507 collection, sample #64758) of composition $[Mg_{0.42}Fe_{0.44}Ca_{0.13}Mn_{0.01}]_3Al_2Si_3O_{12}$ as obtained by
508 EPMA with Fe^{2+}/Fe_{total} assumed to be 1.00. However, the ^{27}Al and ^{29}Si spectra showed simply a
509 single very broad peak (>100 ppm FWHM) and the manifold of associated spinning sidebands.
510 This was observed even at a spinning speed of 23 kHz and a field of 14.1 T, which were used in
511 an attempt to separate spinning sidebands from the isotropic resonance. The central peaks were
512 so broad for both nuclides that their positions could not be determined. Nonetheless, the results
513 of this experiment place an approximate upper limit on the almandine component that can be
514 present in garnet, beyond which no informative MAS NMR spectra can be measured. Lower
515 fields and/or faster spinning speeds could extend this range somewhat.
516

Implications and future work

Based on the results of this investigation, we show that it is possible to collect interpretable and informative ^{27}Al and ^{29}Si MAS NMR spectra of garnets with up to a 25 mol% almandine component (up to 12.6 wt% FeO). NMR spectra have also been collected on Fe- or Mn-rich oxide/hydroxides (Kim et al. 2008; Nielsen et al. 2008; Kim et al. 2011; Nielsen et al. 2011) and other materials of technological importance in which Fe, Mn, or other transition metal cations are major components (c.f. Middlemiss et al. 2013). Other aspects of the challenges of applying NMR to Fe-bearing silicates have been described recently (c.f. Bégaudeau et al. 2012). However, MAS NMR ^{27}Al and ^{29}Si spectra of common silicate minerals with similarly high concentrations of paramagnetic species are rare. In fact, an early ^{29}Si MAS NMR study of forsterite-rich olivine with a 5 mol% fayalite component [$(Mg_{0.95}Fe_{0.05})_2SiO_4$, 5.0 wt.% FeO] found no discernible paramagnetically shifted peaks. Only a single resonance, shifted slightly from that of pure forsterite but with ~20 ppm line broadening was observed (Grimmer et al. 1983). The authors reported, furthermore, the absence of any NMR signal for an olivine with 8.8 wt.% FeO. In our study, grossular G12 and pyrope P6 with a 25 mol% almandine component (11.7 and 12.6 wt.% FeO, respectively) show ^{29}Si MAS NMR peaks with 40-50 ppm line broadening, roughly scaling with the peak broadening relative to wt.% FeO observed in the spectrum of olivine of Grimmer et al. (1983). However, in the case of garnet, there are three discernible peaks relating to three different local SiO_4-XO_8 configurations (X = Ca-Fe^{2+} or Mg-Fe^{2+}). Therefore, the featureless spectrum of the $(Mg_{0.95}Fe_{0.05})_2SiO_4$ olivine is probably not simply a result of severe line broadening related to paramagnetic effects on nuclear relaxation. Because olivine, of orthorhombic symmetry, has a larger number of local SiO_4-MO_6 configurations, involving two crystallographically independent octahedral M-sites, its NMR

spectra should show more paramagnetically shifted peaks than in the case of garnet. In other words, Fe-bearing olivines have many ^{29}Si NMR resonances leading to a loss of spectral resolution at high concentrations of Fe^{2+}. In fact, McCarty et al. (2012, 2014) have demonstrated the presence of a large number of paramagnetically shifted peaks in high-resolution ^{29}Si MAS NMR spectra of synthetic Mg_2SiO_4 forsterite with small concentrations, less than 1 mol%, of a Fe_2SiO_4 component. Thus, NMR studies on minerals containing paramagnetic transition metals or rare earth elements must consider the crystal structure and the number of possible local atomic configurations around the target NMR nuclide.

Finally, while it is surprising that ^{27}Al and ^{29}Si MAS NMR spectra can be recorded for garnets with up to 12.6 wt.% FeO, it is important to put this finding in the context of what can be determined regarding local structural properties. In particular, if an appropriate suite of garnets were procured, the methodology developed in this study could be used to address two important problems, namely, 1) The presence or absence of tetrahedral Al and 2) The state of short-range order/disorder of X-site cations in garnets with roughly less than 50 mol% almandine. Both questions are important for understanding the precise crystal chemistry and thermodynamics of garnet. The detection of subtle structural features described herein may put MAS NMR spectroscopy in a unique position to help resolve both of these questions. In fact, the large separation in frequency between paramagnetically shifted peaks seen here may actually allow for a higher level of structural information when considering the question of short-range ordering by increasing the resolution between distinct atomic configurations. The methodology described in this study may also be used to shed light on questions beyond that of short-range ordering such as site occupancy and intracrystalline partitioning of minor to trace elements. The gaining momentum in the application of NMR spectroscopy to paramagnetic geologic materials is set to

take advantage of the potential for future work on a wide variety of silicate and non-silicate minerals.

Acknowledgements

This work was supported by grants from the National Science Foundation (EAR-1019516, Stebbins) and the Austrian Science Fund (FWF, P 25597-N20, Geiger). We thank Sarah Roeske and Nick Botto at the University of California, Davis and Bob Jones at Stanford University for help with the EPMA. The following individuals and institutions kindly provided samples for study: George R. Rossman (Caltech, Pasadena, G1), Michel Picard (Canadian Museum of Nature, Ottawa, G5/CMNMC 48324), and Christian Chopin (École Normale Supérieure, Paris, P4/Mas-2 and P5/SB-1). We thank an anonymous reviewer and the Associate Editor, Yann Morizet, who also reviewed the paper, for their very helpful and constructive comments.

References Cited

Allen, F.M. and Buseck, P.R. (1988) XRD, FTIR, and TEM studies of optically anisotropic grossular garnets. American Mineralogist, 73, 568-584.

Amthauer, G., Annersten, H., and Hafner, S.S. (1976) The Mössbauer spectrum of ^{57}Fe in silicate garnets. Zeitschrift der Kristallographie, 143, 14-55.

Armbruster, T., Geiger, C.A., Lager, G.A. (1992) Single-crystal X-ray structure study of synthetic pyrope almandine garnets at 100 and 293 K. American Mineralogist, 77, 512-521.

Armbruster, T. and Geiger, C.A. (1993) Andradite crystal chemistry, dynamic X-site disorder and structural strain in silicate garnets. European Journal of Mineralogy, 5, 59-71.

Bach, W. and Klein, F. (2009) The petrology of seafloor rodingites: Insights from geochemical reaction path modeling. Lithos, 112, 103-117.

Baxter, E.F., Caddick, M.J., and Ague, J.J., Eds. (2013) Garnet: Common mineral, uncommonly useful. Elements, 9, 415-456.

Bégaudeau, K., Morizet, Y., Paris, M., Florian, P., Lévêque, F., and Mercier, J. (2012) Solid-state NMR analysis of Fe-bearing minerals: implications and applications for Earth sciences. European Journal of Mineralogy, 24, 535-550.

Bertini, I.B., Luchinat, C., Parigi, G., and Pieratelli, R. (2005) NMR spectroscopy of paramagnetic metalloproteins. ChemBioChem, 6, 1536-1549.

Boffa Ballaran T., Carpenter, M.A., Geiger, C.A., and Koziol, A. (1999) Local structural heterogeneity in garnet solid solutions. Physics and Chemistry of Minerals, 26, 554-569.

Bosenick, A., Geiger, C.A., Schaller, T., and Sebald, A. (1995) A ^{29}Si MAS NMR and IR

spectroscopic investigation of synthetic pyrope-grossular garnet solid solutions. American Mineralogist, 80, 691-704.

Bosenick, A. Geiger, C.A., and Phillips, B.L. (1999) Local Ca-Mg distribution of Mg-rich pyrope-grossular garnets synthesized at different temperatures revealed by ^{29}Si MAS NMR spectroscopy. American Mineralogist, 84, 1422-1432.

Bosenick, A., Dove, M.T., and Geiger, C.A. (2000) Simulation studies on the pyrope-grossular garnet solid solution. Physics and Chemistry of Minerals, 27, 398-418.

Brinkmann, D. and Kaeser, L. (1972) Hyperfine interactions of Al and Si in the paramagnetic garnet almandine $(Fe,Mg)_3Al_2(SiO_4)_3$. Solid State Communications, 11, 1519-1521.

Cho, H. and Rossman, G.R. (1993) Single-crystal NMR studies of low-concentration hydrous species in minerals: Grossular garnet. American Mineralogist, 78, 1149-1164.

Dachs, E., Geiger, C.A., Benisek, A., and Grevel, K.-D. (2012) Grossular: A crystal-chemical, calorimetric, and thermodynamic study. American Mineralogist, 97, 1299-1313.

Dajda, N., Dixon, J.M., Smith, M.E., Carthey, N., and Bishop, P.T. (2003) Atomic site preferences and structural evolution in vanadium-doped $ZrSiO_4$ from multinuclear solid-state NMR. Physical Review B, 67, 024201.

Deer, W.A., Howie, R.A., and Zussman, J. (1992) An Introduction to the Rock-Forming Minerals, 2nd ed. Longman Scientific and Technical, New York.

Freeman, C.L., Allan, N.L., and van Westrenen, W. (2006) Local cation environments in the pyrope–grossular $Mg_3Al_2Si_3O_{12}$–$Ca_3Al_2Si_3O_{12}$ garnet solid solution. Physical Review B, 74, 134203.

620 Geiger, C.A. (1998) A powder infrared spectroscopic investigation of garnet binaries in the
621 system $Mg_3Al_2Si_3O_{12}$-$Fe_3Al_2Si_3O_{12}$-$Mn_3Al_2Si_3O_{12}$-$Ca_3Al_2Si_3O_{12}$. European Journal of
622 Mineralogy, 3, 407-422.
623 ——— (2013) Garnet: A key phase in nature, the laboratory, and technology. Elements, 9, 447-
624 452.
625 Geiger, C.A. and Armbruster, T. (1997) $Mn_3Al_2Si_3O_{12}$ spessartine and $Ca_3Al_2Si_3O_{12}$ grossular
626 garnet: Structural dynamic and thermodynamic properties. American Mineralogist, 82,
627 740-747.
628 Geiger, C.A. and Rossman, G.R. (1994) Crystal field stabilization energies of almandine-pyrope
629 and almandine-spessartine garnets determined by FTIR near infrared measurements.
630 Physics and Chemistry of Minerals, 21, 516-525.
631 Geiger, C.A. and Feenstra, A. (1997) Molar volumes of mixing of almandine-pyrope and
632 almandine-spessartine garnets and the crystal chemistry of aluminosilicate garnets.
633 American Mineralogist. 82, 571-581.
634 Geiger, C.A., Newton, R.C., and Kleppa, O.J. (1987) Enthalpy of mixing of synthetic almandine-
635 grossular and almandine-pyrope garnets from high temperature solution calorimetry.
636 Geochimica et Cosmochimica Acta. 51, 1755-1763.
637 Geiger, C.A., Armbruster, T., Lager, G.A., Jiang, K., Lottermoser, W., and Amthauer, G. (1992)
638 A combined temperature dependent Mössbauer and single crystal X-ray diffraction study
639 of synthetic almandine: Evidence for the Gol`danskii-Karyagin effect. Physics and
640 Chemistry of Minerals. 19, 121-126.
641 Geiger, C.A., Grodzicki, M., and Amthauer, G. (2003) The crystal chemistry and Fe^{II} site
642 properties of aluminosilicate garnet solid solutions as revealed by Mössbauer

643 spectroscopy and electronic structure calculations. Physics and Chemistry of Minerals.
644 30, 280-292.
645 Geiger, C.A., Brearley, A.J., Dachs, E., Tippelt, G. (2013) Almandine: Crystal chemistry,
646 defects, inclusions and physical properties. American Geophysical Union, Fall Meeting
647 2013, V51B-2653.
648 Griffen, D.T., Hatch, D.M., Phillips, W.R., and Kulaksiz, S. (1992) Crystal chemistry and
649 symmetry of a birefringent tetragonal pyralspite$_{75}$-grandite$_{25}$ garnet. American
650 Mineralogist, 77, 399-406.
651 Grimmer, A.-R., von Lampe, F., Mägi, M., Lippmaa, E. (1983) Hochauflösende ^{29}Si-NMR an
652 festen Silicaten; Einfluß von Fe^{2+} in Olivinen. Zeitschrift für Chemie, 23, 343-344.
653 Huggins, F.E., Virgo, D., and Huckenholz, H.G. (1977) Titanium-containing silicate garnets. II.
654 The crystal chemistry of melanites and schorlomite. American Mineralogist, 62, 646-665.
655 Janes, N. and Oldfield, E. (1985) Prediction of silicon-29 nuclear magnetic resonance chemical
656 shifts using a group electronegativity approach: applications to silicate and
657 aluminosilicate structures. Journal of the American Chemical Society, 107, 6769-6775.
658 Kelsey, K.E., Stebbins, J.F., Du, L-S., and Hankins, B. (2007) Constraining ^{17}O and ^{27}Al NMR
659 spectra of high-pressure crystals and glasses: New data for jadeite, pyrope, grossular, and
660 mullite. American Mineralogist, 92, 210-216.
661 Kim, N., Stebbins, J.F., Quartieri, S., and Oberti, R. (2007) Scandium-45 NMR of pyrope-
662 grossular garnets: Resolution of multiple scandium sites and comparison with X-ray
663 diffraction and X-ray absorption spectroscopy. American Mineralogist, 92, 1875-1880.
664 Kim, J., Nielsen, U.G., and Grey, C.P. (2008) Local environments and lithium adsorption on the

665 iron oxyhydroxides lepidocrocite (γ-FeOOH) and goethite (α-FeOOH): A ^{2}H and ^{7}Li
666 solid-state MAS NMR study. Journal of the American Chemical Society, 130, 1285-
667 1295.
668 Kim, J., Li, W., Philips, B.L., and Grey, C.P. (2011) Phosphate adsorption on the iron
669 oxyhydroxides goethite (α-FeOOH), akaganeite (β-FeOOH), and lepidocrocite (γ-
670 FeOOH): a ^{31}P NMR Study. Energy & Environmental Science, 4, 4298-4305.
671 Kingma, K.J. and Downs, J.W. (1989) Crystal-structure analysis of a birefringent andradite.
672 American Mineralogist, 74, 1307-1316.
673 Ma, C. and Krot, A.N. (2014) Hutcheonite, $Ca_3Ti_2(SiAl_2)O_{12}$, a new garnet mineral from the
674 Allende meteorite: An alteration phase in a Ca-Al-rich inclusion. American Mineralogist,
675 99, 667-670.
676 McCarty, R.J., Palke, A.C., Stebbins, J.F., and Hartman, S. (2012) A ^{29}Si MAS-NMR study of
677 transition metal site occupancy in forsterite. American Geophysical Union, Fall Meeting
678 2012, MR11A-2470.
679 McCarty, R.J., Palke, A.C., and Stebbins, J.F. (2014) The site preference and distribution of low
680 concentration elements in forsterite as determined by NMR. Goldschmidt Conference
681 2014.
682 Merli, M., Callegari, A., Cannillo, E., Caucia, F., Leona, M., Oberti, R., and Ungaretti, L. (1995)
683 Crystal-chemical complexity in natural garnets: structural constraints on chemical
684 variability. European Journal of Mineralogy. 7, 1239-1249.
685 Middlemiss, D.S., Ilott, A.J., Clement, R.J., Strobridge, F.C., and Grey, C.P. (2013) Density

functional theory-based bond pathway decompositions of hyperfine shifts: equipping solid-state NMR to characterize atomic environments in paramagnetic materials. Chemistry of Materials, 25, 1723-1734.

Nielsen, U.G., Majzlan, J., and Grey, C.P. (2008) Determination and quantification of the local environments in stoichiometric and defect jarosite by solid-state ^{2}H NMR spectroscopy. Chemistry of Materials, 20, 2234-2241.

Nielsen, U.G., Heinmaa, I., Samoson, A., Majzlan, J., and Grey, C.P. (2011) Insight into the local magnetic environments and deuteron mobility in jarosite ($AFe_3(SO_4)_2(OD,OD_2)_6$, A = K, Na, D_3O) and hydronium alunite ($(D_3O)Al_3(SO_4)_2(OD)_6$), from variable-temperature ^{2}H MAS NMR Spectroscopy. Chemistry of Materials, 23, 3176-3187.

Normand, C. and Williams-Jones, A.E. (2007) Physicochemical conditions and timing of rodingite formation: evidence from rodingite-hosted fluid inclusions in the JM asbestos mine, Asbestos, Québec. Geochemical Transactions, 8:11.

Oldfield, E., Kinsey, R.A., Smith, K.A., Nichols, J.A., and Kirkpatrick, R.J. (1983) High-resolution NMR of inorganic solids. Influence of magnetic centers on magic-angle sample-spinning lineshapes in some natural aluminosilicates. Journal of Magnetic Resonance, 51, 325-329.

Palke, A.C. and Stebbins, J.F. (2011) Variable temperature ^{27}Al and ^{29}Si NMR studies of synthetic forsterite and Fe-bearing Dora Maira pyrope garnet: temperature dependence and mechanisms of paramagnetically-shifted peaks. American Mineralogist, 96, 1090-1099.

Palke, A.C., Stebbins, J.F., Frost, D.J., and McCammon, C.A. (2012) Incorporation of Fe and Al in $MgSiO_3$ perovskite: An investigation by ^{27}Al and ^{29}Si NMR spectroscopy. American

709 Mineralogist, 97, 1955-1964.

710 Palke, A.C., Stebbins, J.F., and Boatner, L.A. (2013) ^{31}P magic angle spinning NMR study of
711 flux-grown rare-earth element orthophosphate (monazite/xenotime) solid solutions:
712 evidence of random cation distribution from paramagnetically shifted NMR resonances.
713 Inorganic Chemistry, 52, 12605-12615.

714 Phillips, B.L., Howell, D.A., Kirkpatrick, R.J., and Gasparik, T. (1992) Investigation of cation
715 order in $MgSiO_3$-rich garnet using ^{29}Si and ^{27}Al MAS NMR spectroscopy. American
716 Mineralogist, 77, 704-712.

717 Redhammer, G.J., Amthauer, G., Lottermoser, W., Bernroider, M., Tippelt, G., and Roth, G.
718 (2005) X-ray powder diffraction and ^{57}Fe-Mössbauer spectroscopy of synthetic
719 trioctahedral micas $\{K\}[Me_3]\langle TSi_3\rangle O_{10}(OH)_2$, Me = Ni^{2+}, Mg^{2+}, Co^{2+}, Fe^{2+}; T = Al^{3+},
720 Fe^{3+}. Mineralogy and Petrology, 85, 89-115.

721 Schingaro, E., Scordari, F., Capitanio, F., Parodi, G., Smith, D.C., and Mottana, A. (2001)
722 Crystal chemistry of kimzeyite from Anguillara, Mts. Sabatini, Italy. European Journal of
723 Mineralogy, 13, 749-759.

724 Shannon, R.D. (1976) Revised effective ionic radii and systematic studies of interatomic
725 distances in halides and chalcogenides. Acta Crystallographica, A32, 751-767.

726 Shannon, R.D. and Rossman, G.R. (1992) Dielectric constants of silicate garnets and the oxide
727 additivity rule. American Mineralogist, 77, 94-100.

728 Sherriff, B.L. and Hartman, J.S. (1985) Solid-state high-resolution ^{29}Si NMR of feldspars: Al-Si
729 disorder and the effects of paramagnetic centres. Canadian Mineralogist, 23, 205-212.

730 Stebbins, J.F. and Kelsey, K.E. (2009) Anomalous resonances in ^{29}Si and ^{27}Al NMR spectra of

731 pyrope ($[Mg,Fe]_3Al_2Si_3O_{12}$) garnets: effects of paramagnetic cations. Physical Chemistry
732 Chemical Physics, 11, 6906-6917.
733 Takéuchi, Y., Haga, N., Umizu, S., and Sato, G. (1982) The derivative structure of silicate
734 garnets in grandite. Zeitschrift für Kristallographie, 158, 53-99.
735 Vinograd, V.L., Sluiter, M.H.F., Winkler, B., Putnis, A., Hålenius, U., Gale, J.D., and Becker, U.
736 (2004) Thermodynamics of mixing and ordering in pyrope–grossular solid solution.
737 Mineralogical Magazine, 68, 101-121.
738 Vinograd, V.L. and Sluiter, M.H.F. (2006) Thermodynamics of mixing in pyrope-grossular,
739 $Mg_3Al_2Si_3O_{12}$-$Ca_3Al_2Si_3O_{12}$, solid solution from lattice dynamics calculations and Monte
740 Carlo simulations. American Mineralogist, 91, 1815-1830.
741 Whitney, D.L. and Evans, B.W. (2010) Abbreviations for names of rock-forming minerals.
742 American Mineralogist, 95, 185-187.
743 Wildner, M. and Andrut, M. (2001) The crystal chemistry of birefringent natural uvarovites: Part
744 II. Single-crystal X-ray structures. American Mineralogist, 86 1231-1251.

745 **Figure Captions**

746 **Figure 1.** Room temperature Mössbauer spectra of samples G5-$Grs_{98.5}Alm_{0.8}And_{0.6}$, G6-
747 $Grs_{96.8}Alm_{1.2}And_{2.0}$, G9-$Grs_{96.7}Alm_{2.9}And_{0.4}$, and G10-$Grs_{91.2}And_{8.8}$. Solid lines are fits to the
748 data with the two-doublet model as described in the text.

749

750 **Figure 2a.** Local coordination relationships between a central AlO_6 octahedron and XO_8
751 dodecahedra in pyrope-rich (X = Mg) and grossular-rich (X = Ca) garnets. Al is depicted by the
752 central black sphere and X-site cations by the cross-hatched spheres. Bonds between cations and
753 oxygen are shown by gray sticks.

754

755 **Figure 2b.** Local coordination relationships between a SiO_4 tetrahedron and XO_8 dodecahedra
756 only two bonds away (i.e. Si-O-X) in pyrope-rich (X = Mg) and grossular-rich (X = Ca) garnets.
757 Si is depicted by the central gray sphere and tetrahedron. XO_8 dodecahedra edge-shared to the
758 SiO_4 tetrahedron are shown by the cross-hatched circles while those sharing corners with the
759 SiO_4 tetrahedron by black circles. Bonds between cations and oxygen are shown by gray sticks.

760

761 **Figure 2c.** Local coordination relationships between a SiO_4 tetrahedron and XO_8 dodecahedra up
762 to four bonds away (i.e. Si-O-X-O-X) in pyrope-rich (X = Mg) and grossular-rich (X = Ca)
763 garnets. Si is depicted by the central gray circle and tetrahedron. The Si atom "sees" three
764 symmetrically inequivalent types of XO_8 dodecahedra in this coordination shell shown by the
765 black, cross-hatched, and two-toned circles. XO_8 dodecahedra edge-shared and corner-shared to
766 the SiO_4 tetrahedron are shown by white circles (see **Figure 2b**). Bonds between cations and
767 oxygen are shown by gray sticks.

768

769 **Figure 3.** ^{27}Al NMR spectra (9.4 T) of pyrope-rich garnets P2-$Prp_{93.3}Alm_{6.7}$, P4-$Prp_{88.0}Alm_{12.0}$,
770 and P5-$Prp_{83.2}Alm_{16.8}$ showing the main unshifted pyrope peak, A0, and paramagnetically shifted
771 peaks A1, A2, and A3. Spinning sidebands are marked by "*".

772

773 **Figure 4a.** ^{27}Al NMR peak widths (14.1 T) vs. Fe_{total} + Mn in atoms per formula unit (afu) for
774 grossular-rich garnets in this study. Note that only those samples with homogenous compositions
775 are included here. Estimated uncertainties for peak widths are ± 5 % of full width at half
776 maximum (FWHM).

777

778 **Figure 4b.** ^{29}Si NMR peak widths vs. Fe_{total} + Mn in atoms per formula unit (afu). Closed circles
779 represent grossular garnets and open circles represent pyrope garnets. Note that only those
780 samples with homogeneous compositions are included here. Estimated uncertainties for peak
781 widths are ± 5 % of full width at half maximum (FWHM).

782

783 **Figure 5.** ^{27}Al NMR spectra (18.8 T) of grossular-rich garnets G7-$Grs_{96.9}Alm_{1.5}And_{1.6}$, G9-
784 $Grs_{96.7}Alm_{2.9}And_{0.4}$, G10-$Grs_{91.2}And_{8.8}$, and G11-$Grs_{90.0}Alm_{10.0}$ and the ^{27}Al NMR spectrum (9.4
785 T) of grossular-rich garnet G12-$Grs_{75.2}Alm_{24.8}$. A portion of the spectrum of G7 is shown with an
786 enlarged vertical scale to emphasize the presence of tetrahedral Al at 60 ppm. Paramagnetically
787 shifted peak "A1" is marked for sample G11.

788

789 **Figure 6a.** ^{29}Si NMR spectra (9.4 T) of grossular-rich garnets G7-$Grs_{96.9}Alm_{1.5}And_{1.6}$ and G8-
790 $Grs_{95.4}And_{4.6}$ as well as pyrope-rich garnet P1-$Prp_{97.3}Alm_{2.7}$ centered around the main, unshifted

grossular or pyrope peaks. Paramagnetically shifted peaks are marked as "S1" and "S2" and the spectrum of G7 is shown with an enlarged vertical scale to emphasize these features.

Figure 6b. ^{29}Si NMR spectra (9.4 T) of grossular-rich garnet G7-$Grs_{96.9}Alm_{1.5}And_{1.6}$ and pyrope-rich garnet P1-$Prp_{97.3}Alm_{2.7}$ showing paramagnetically shifted peak S4. Both spectra are also shown with an enlarged vertical scale to bring out this feature. Spinning sidebands are marked with "*" for the main band of resonances and "*S4*" for peak S4.

Figure 7. Results of the fitting procedure of the main band of resonances from the ^{29}Si NMR spectrum of grossular garnet G7-$Grs_{96.9}Alm_{1.5}And_{1.6}$ showing individual contributions from specific resonances described in the text. "S1" and "S2" refer to paramagnetically shifted peaks while "USN" and "USB" refer to the narrow and broad component needed to fit the main, unshifted peak. The experimental spectrum is shown above the "SUM" of the fitted components with the residual to the fit at the bottom.

Figure 8a. ^{29}Si NMR spectrum (9.4 T) collected with a spin echo pulse sequence for pyrope-rich garnets P4-$Prp_{88.0}Alm_{12.0}$, and P5-$Prp_{83.2}Alm_{16.8}$, and P6-$Prp_{73.7}Alm_{26.3}$ with relatively large almandine components. The main band of resonances is shown at about -70 to -90 ppm. Peaks S1 and S2 are observed and labeled for P4 but not for the other samples.

Figure 8b. ^{29}Si NMR spectrum (9.4 T) collected with a spin echo pulse sequence for grossular-rich garnet G12-$Grs_{75.2}Alm_{24.8}$ with a relatively large almandine component. The main band of

resonances is shown at about -105 ppm. Note the wider frequency scale range compared to **Figure 8a**.

Figure 9. ^{29}Si NMR spectrum (9.4 T) collected with a spin echo pulse sequence for pyrope-rich garnets P4-$Prp_{88.0}Alm_{12.0}$, P5-$Prp_{83.2}Alm_{16.8}$, P6-$Prp_{73.7}Alm_{26.3}$, and grossular-rich garnet G12-$Grs_{75.2}Alm_{24.8}$. The spectra highlight the main band of resonances at about -70 to -100 ppm, peak S4 at about +100 to +130 ppm, and peak S4+S4 at about +330 ppm. Simplified atomic diagrams are presented above each peak showing their relationship to configurations of SiO_4 tetrahedra with zero, one, or two Fe^{2+} in edge-shared X-sites. Spectra of P4 and P5 are shown as well with the vertical scale enlarged 5× to highlight low-intensity features. *S0*, *S4*, and *S4+S4* mark the respective spinning sidebands.

Table 1a. Grossular compositions from EPMA with Fe^{2+}/Fe_{total} from Mössbauer analysis

		G1	G2	G3	G4	G5	G6	G7	G8	G9	G10	G11	G12
X site	Ca	3.013	2.989	3.014	3.008	2.979	2.908	2.974	2.933	2.894	2.983	2.700	2.278
	Mg	0.031	0.038	0.003	0.002	0.001	0.041	0.000	0.003	0.001	0.086	0.000	0.000
	Mn^{2+}	0.009	0.023	0.005	0.007	0.012	0.026	0.000	0.000	0.029	0.006	0.000	0.000
	Fe^{2+}	0.000	0.007	0.016	0.014	0.025	0.035	0.044	0.000	0.087	0.000	0.300	0.753
	total	3.054	3.057	3.039	3.030	3.017	3.009	3.018	2.936	3.010	3.075	3.000	3.031
Y site	Al	1.963	1.974	1.990	1.967	1.991	1.906	2.030	1.963	1.955	1.764	2.000	2.009
	Fe^{3+}	0.009	0.014	0.010	0.013	0.012	0.041	0.033	0.091	0.007	0.176	0.000	0.000
	total	1.973	1.987	2.000	1.979	2.003	1.946	2.063	2.054	1.962	1.940	2.000	2.009
Z site	Si	2.966	2.985	2.983	2.992	2.979	3.008	2.947	2.991	3.001	3.011	3.000	2.977
	Ti	0.030	0.000	0.000	0.004	0.002	0.031	0.000	0.000	0.000	0.031	0.000	0.000
	total	2.996	2.985	2.983	2.997	2.981	3.039	2.947	2.991	3.002	3.042	3.000	2.977
Mole % garnet end member decomposition	Grossular (Grs)	99.5	99.1	99.0	98.9	98.5	96.8	96.9	95.6	96.7	90.9	90.0	75.2
	Almandine (Alm)	0.0	0.2	0.5	0.5	0.8	1.2	1.5	0.0	2.9	0.0	10.0	24.8
	Andradite (Adr)	0.5	0.7	0.5	0.6	0.6	2.0	1.6	4.4	0.4	9.1	0.0	0.0
Paramagnetic species	Fe_{total}	0.009	0.020	0.026	0.027	0.038	0.075	0.077	0.091	0.094	0.176	0.300	0.753
	Fe^{2+}/Fe_{total}	0.000	0.331[1]	0.631[1]	0.520[1]	0.672[1]	0.461[1]	0.573[1]	0.000[1]	0.922[1]	0.000[1]	1.000	1.000
	$Fe_{total} + Mn^{2+}$	0.018	0.043	0.031	0.034	0.050	0.101	0.077	0.091	0.123	0.182	0.300	0.753
Alternative label/ Literature citations		*GRR1386* Cho and Rossman (1993) *Gr2* Shannon and Rossman (1992)	*Gr1/1* Dachs et al. (2012)	82/112 Dachs et al. (2012)	*Gr7/2*	*CMNMC 48324*	*Gr1/4*	-	-	*10074* (Virgin Valley Sales)	*50790*	*Gr90A110* Geiger et al. (1987)	*Gr75A125* Geiger et al. (1987)
Locality		Lelatema Hills, Tanzania	Lualenyi, Kenya?	Jeffrey Mine, Quebec, Canada	Unknown	Jeffrey Mine, Quebec, Canada	Unknown	Synthetic	Synthetic	Jeffrey Mine, Quebec	Lake Jaco, Chihuahua, Mexico	Synthetic	Synthetic

[1]Errors in the Fe^{2+}/Fe_{total} values given by the Mössbauer measurements vary with Fe concentration or ^{57}Fe-enrichment (G7 and G8). Estimated uncertainties are 15-25% for low-Fe samples G2, G3, and G4, 10-15% for G5 and G6, and <5% for G7, G8, G9, and G10.

Table 1b. Pyrope compositions from EPMA

		P1	P2	P3	P4	P5	P6
X site	Ca	0.017	0.048	0.000	0.082	0.106	0.000
	Mg	2.924	2.731	2.700	2.628	2.468	2.173
	Mn^{2+}	0.000	0.005	0.000	0.001	0.003	0.000
	Fe^{2+}	0.081	0.204	0.300	0.358	0.498	0.777
	total	3.022	2.988	3.000	3.069	3.075	2.950
Y site	Al	2.019	2.005	2.000	2.056	2.062	2.023
	Fe^{3+}	0.000	0.000	0.000	0.000	0.000	0.000
	total	2.019	2.005	2.000	2.056	2.062	2.023
Z site	Si	2.972	3.000	3.000	2.922	2.915	3.005
	Ti	0.002	0.003	0.000	0.001	0.001	0.000
	total	2.974	3.003	3.000	2.923	2.916	3.005
Mole % garnet end member decomposition	Pyrope (Prp)	97.3	93.3	90.0	88.0	83.2	73.7
	Grossular (Grs)	0.0	0.0	0.0	0.0	0.0	0.0
	Almandine (Alm)	2.7	6.7	10.0	12.0	16.8	26.3
Paramagnetic species	Fe_{total}	0.081	0.204	0.3	0.358	0.498	0.777
	Fe^{2+}/Fe_{total}	1.000	1.000	1.000	1.000	1.000	1.000
	$Fe_{total} + Mn^{2+}$	0.081	0.209	0.3	0.359	0.501	0.777
Alternative label/ Literature citations		*DW* Stebbins and Kelsey (2009)	*DP* Stebbins and Kelsey (2009)	*Py90Al10* Geiger et al. (1987)	*Mas-2a* Geiger and Rossman (1994)	*SB-1* Geiger and Rossman (1994)	*Py75Al25* Geiger et al. (1987)
Locality		Dora Maira, Italy	Dora Maira, Italy	Synthetic	Masueria, Dora Maira, Italy	San Bernardo, Dora Maira, Italy	Synthetic

Table 2. Concentration of Fe^{2+} (atoms per formula unit) estimated by NMR in comparison to Mössbauer+EPMA measurements

	G1	G2	G3	G4	G5	G6	G7	G8	G9	G10
Fe^{2+} (NMR)	0.000(1)	0.012(2)	0.012(2)	0.012(2)	0.021(3)	0.030(4)	0.045(5)	0.000(1)	0.084(8)	0.000(1)
Fe^{2+} (Mössbauer+EPMA)	-	0.007(2)	0.016(3)	0.014(4)	0.025(3)	0.035(2)	0.044(5)	0.000(1)	0.087(5)	0.000(2)

Figure 1

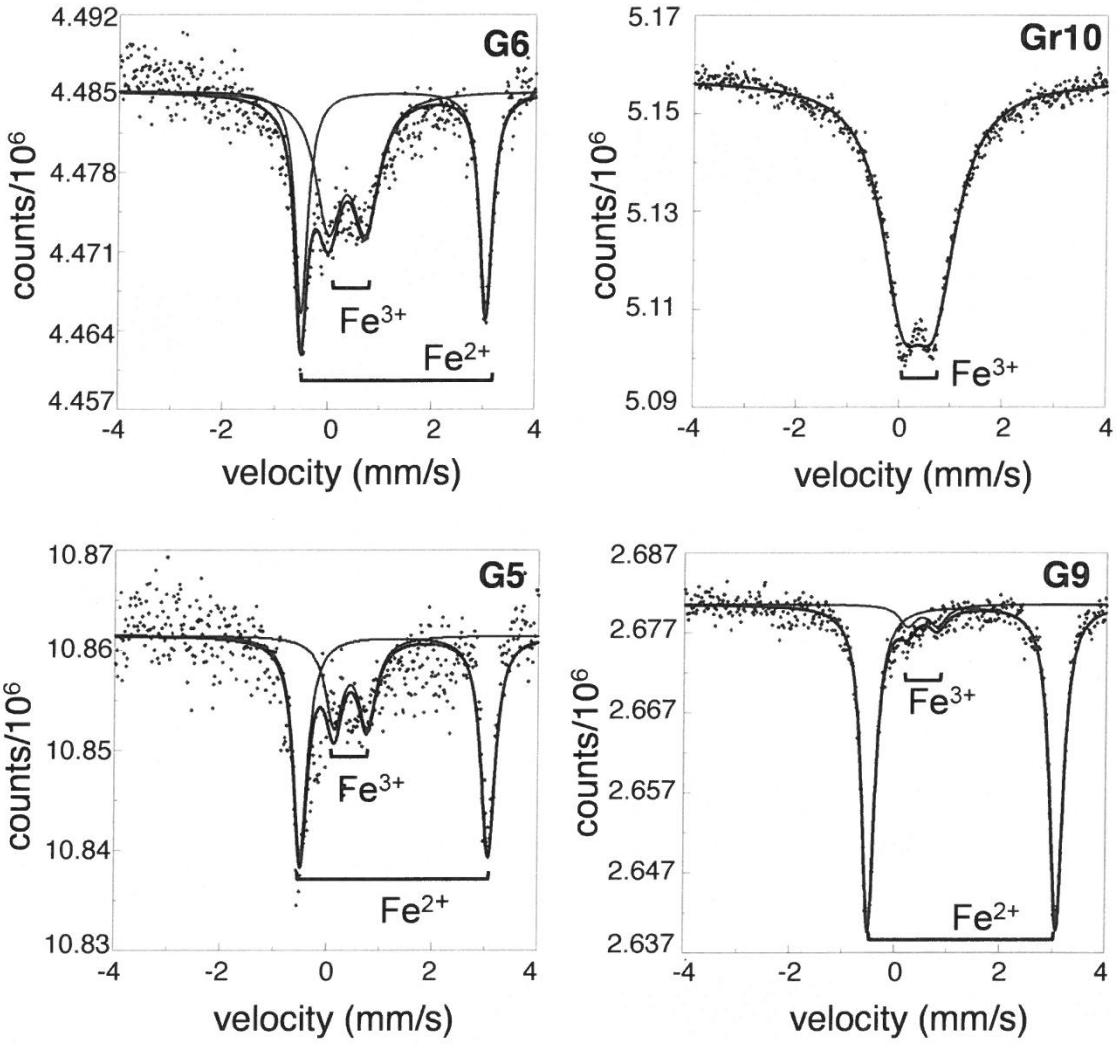
G6
4.492
4.485
4.478
4.471
4.464
4.457
counts/10^6
Fe3+
Fe2+
-4
-2
0
2
4
velocity (mm/s)
Gr10
5.17
5.15
5.13
5.11
5.09
counts/10^6
Fe3+
velocity (mm/s)
G5
10.87
10.86
10.85
10.84
10.83
counts/10^6
Fe3+
Fe2+
velocity (mm/s)
G9
2.687
2.677
2.667
2.657
2.647
2.637
counts/10^6
Fe3+
Fe2+
velocity (mm/s)

Figure 2a

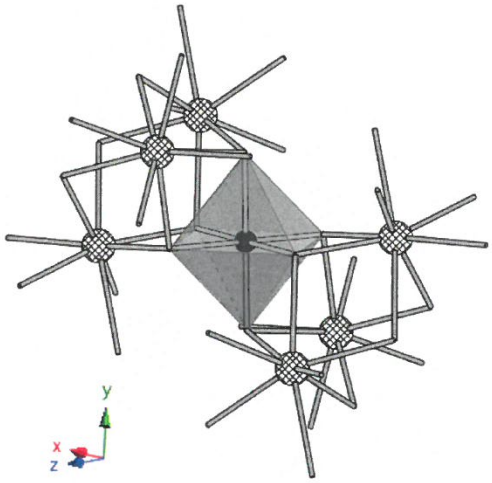

Figure 2b

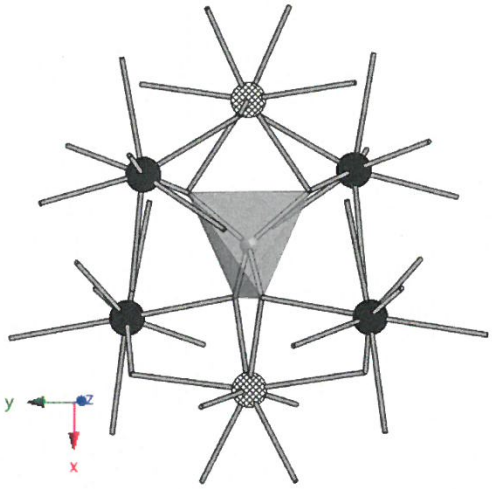

Figure 2c

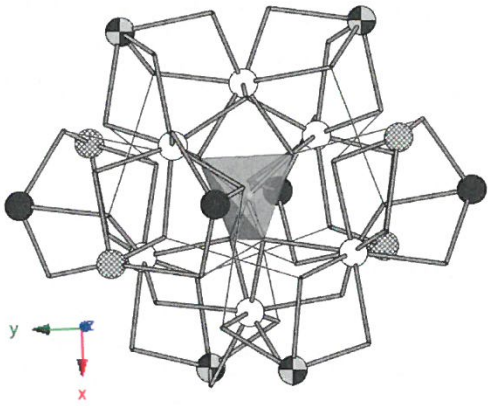

Figure 3

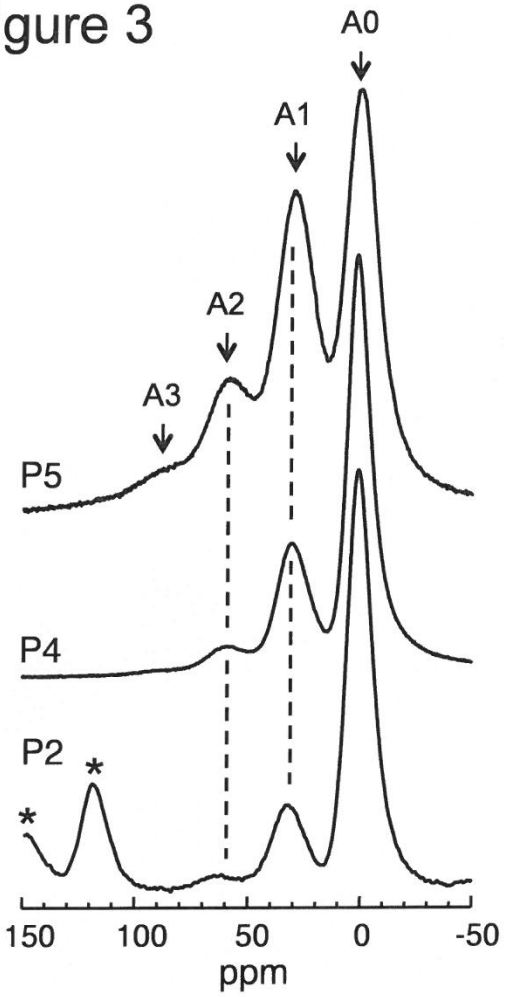

Figure 4a

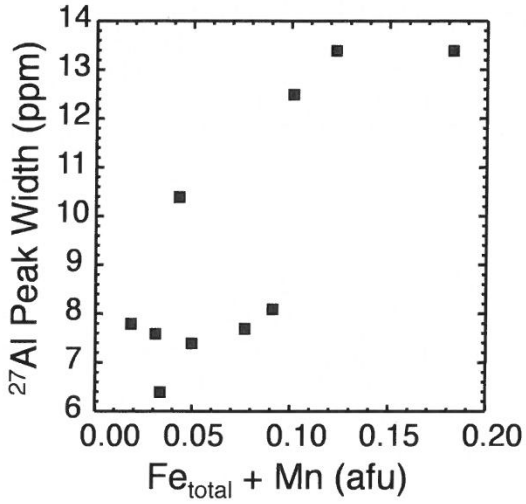
^{27}Al Peak Width (ppm)
14
13
12
11
10
9
8
7
6
0.00
0.05
0.10
0.15
0.20
Fe_{total} + Mn (afu)

Figure 4b

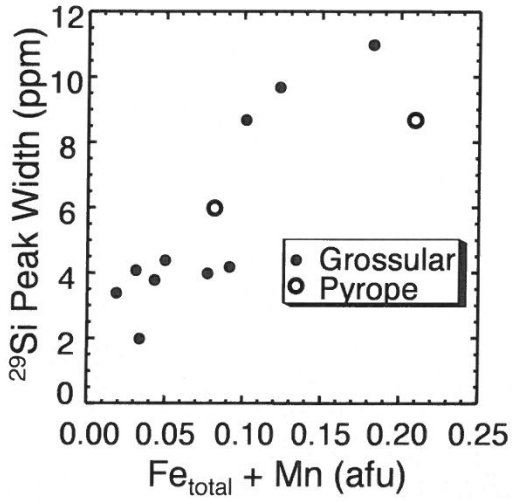
^{29}Si Peak Width (ppm)
12
10
8
6
4
2
0
0.00 0.05 0.10 0.15 0.20 0.25
Fe_{total} + Mn (afu)
Grossular
Pyrope

Figure 5

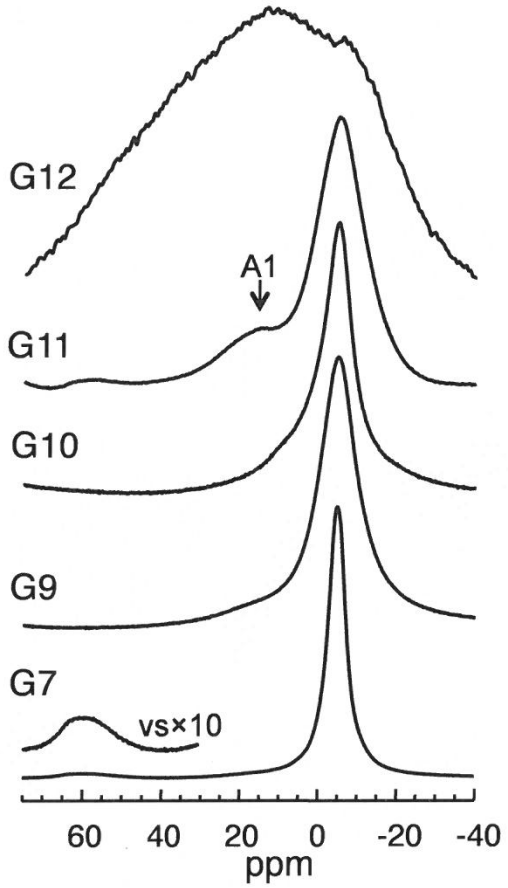

Figure 6a

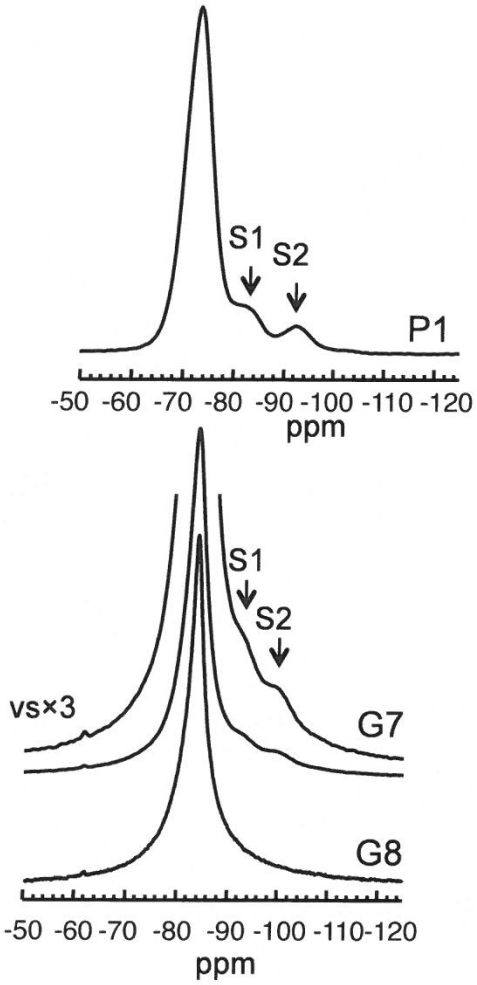
S1
S2
P1
-50 -60 -70 -80 -90 -100 -110 -120
ppm
S1
S2
vs×3
G7
G8
-50 -60 -70 -80 -90 -100 -110-120
ppm

Figure 6b

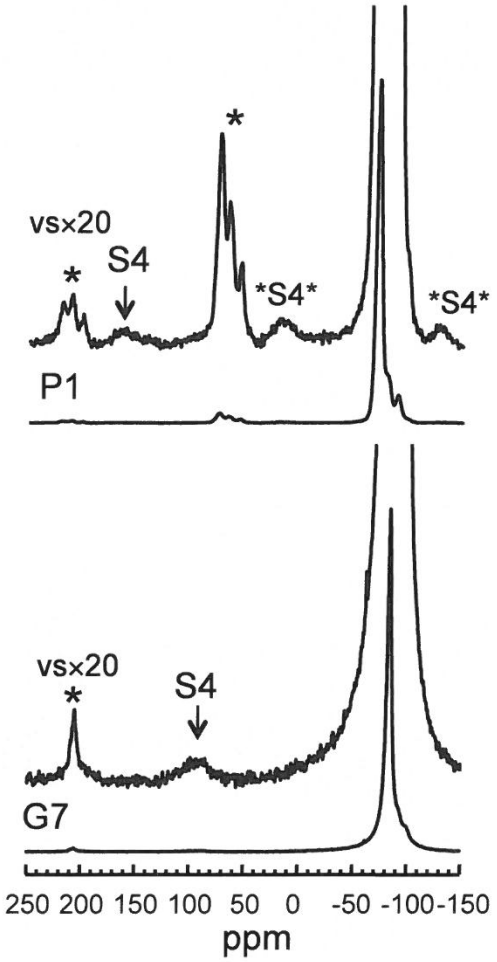

Figure 7

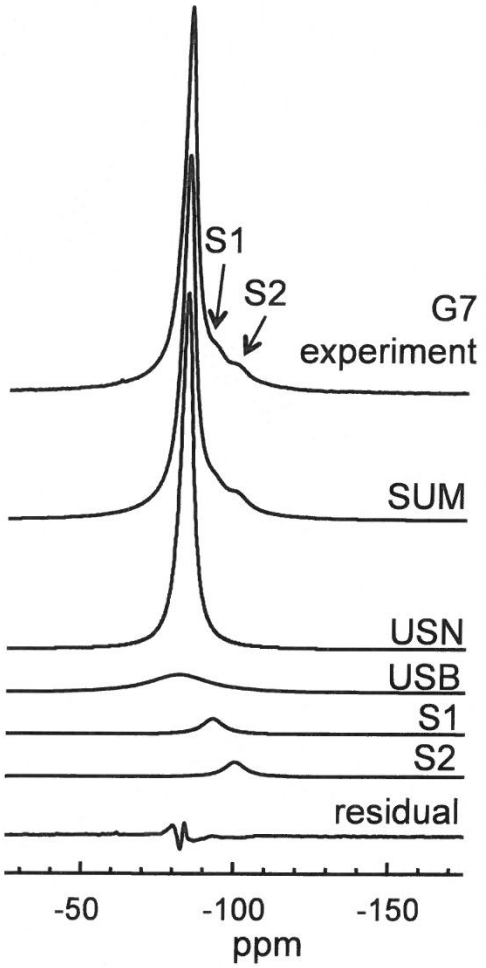

Figure 8a

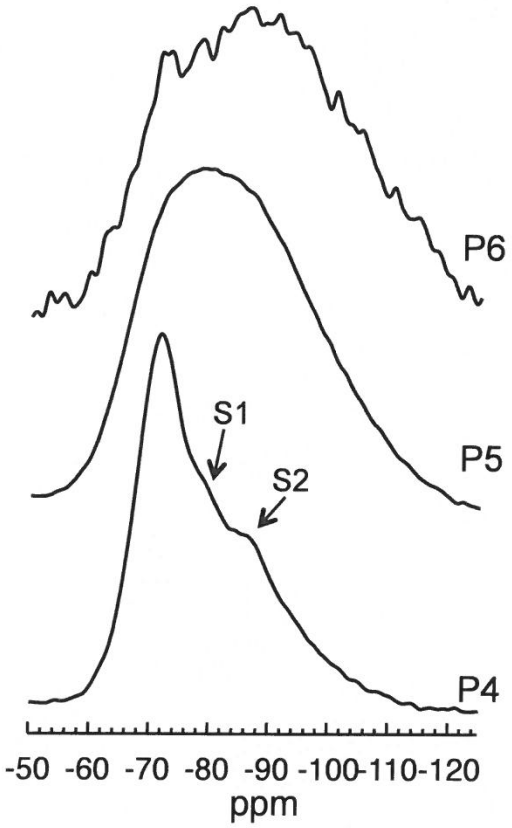

Figure 8b

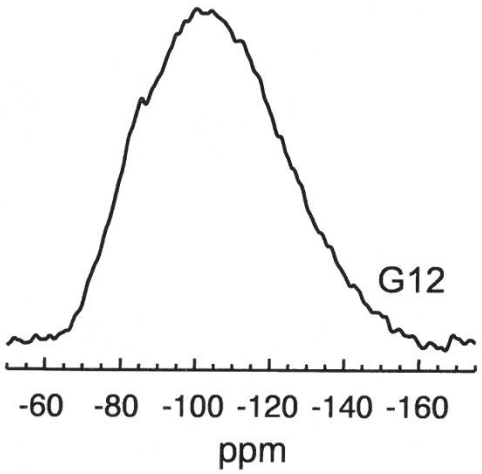

Figure 9

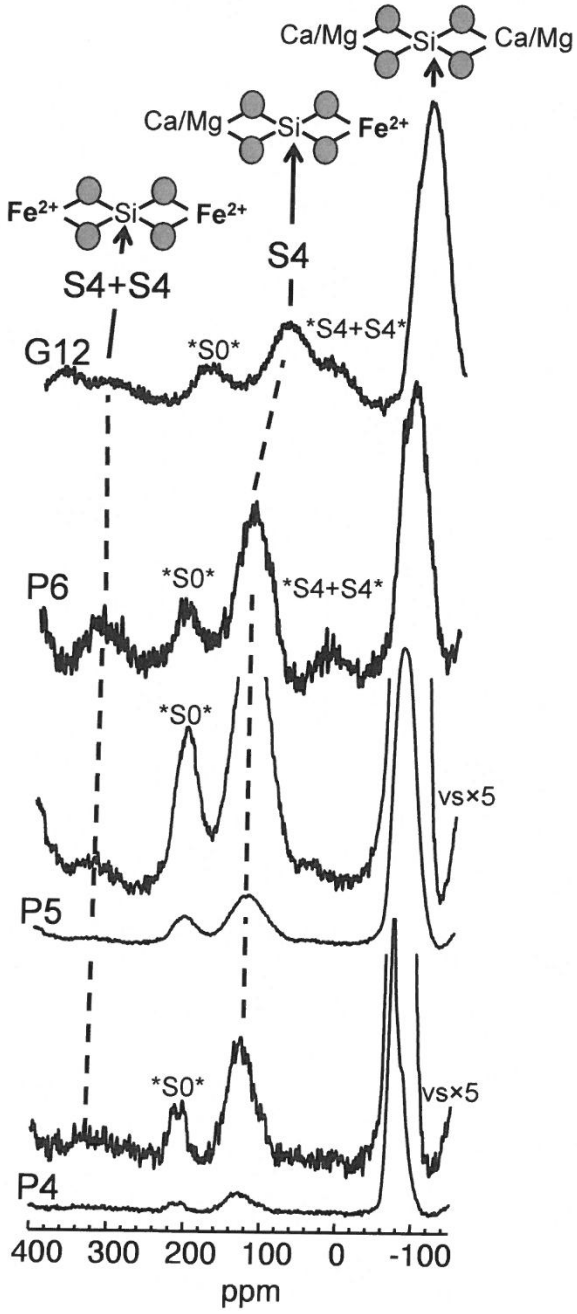
Ca/Mg
Si
Ca/Mg
Ca/Mg
Si
Fe2+
Fe2+
Si
Fe2+
S4+S4
S4
G12
S0
S4+S4
P6
S0
S4+S4
S0
vs×5
P5
S0
vs×5
P4
400 300 200 100 0 -100
ppm